Tele-effect of geomorphological change on the spatial variability of the precision of SfM-MVS 3D point-cloud models

Miao Zhang[1,*], Christopher Gomez[1,2], Norifumi Hotta[3], Rikuto Daikai[1], Sho Sawada[1], Balazs Bradak[1]

[1] Kobe University, Faculty of Oceanology, Laboratory of Sediment Hazards and Disaster Risk, Japan
[2] University Gadjah Mada, Yogyakarta, Pusat Studi Bencana PSBA, Department of Geography, Indonesia
[3] University of Tokyo, Graduate School of Agricultural and Life Science, Japan
* Corresponding author: zhangmiao32@outlook.com

ABSTRACT

Earth-surface processes research is increasingly using the SfM-MVS (Structure from Motion and Multiple-View Stereophotogrammetry) method to model land surface change over time at a very fine-scale. However, the role of topographic change on the error calculated from "stable and fixed" Ground Control Points is under-documented and as far as the authors are aware, it has not been evaluated as yet. Therefore, the present study is an analysis of the variability inherent to the SfM-MVS method used for 3D terrain modeling, in a semi-controlled environment, comparing repeats of measurements, and repeats including topographic change in the laboratory scene, in order to assess the role of elevation change in the scene on the space that remains unchanged. The methodological framework involves varying the terrain morphology by adding 50 and 100 ml of sand to an originally horizontal sandbox, creating a mount in the centre. Then, the authors compared the different experimental surfaces and their repeats acquired by SfM-MVS, and using Gaussian Kernel Density Estimation (KDE). Results demonstrated that under stable and uniform flat surface conditions, the SfM method yields relatively consistent results (standard deviation variety less than 0.027 mm). However, when the experiments included the 50 ml and 100 ml mount of sand, the variability between repeats increased, even for location where no topographic change had occurred. The authors argue that the topographic variability is spreading the error, increasing it compared to the flat experiment. By extension, this consideration is essential, especially for research investigating topographic change such as landslide and other erosion and deposition processes, because the error propagation varies with the surface change, and relating erosion/deposition to topographic change needs to be done carefully.

KEYWORDS

geomorphologic change; point cloud; structure from motion; precision variability; terrain modeling

Received: 16 July 2024
Accepted: 11 February 2025
Published online: 24 March 2025

Zhang, M., Gomez, C., Hotta, N., Daikai, R., Sawada, S., Bradak, B. (2025): Tele-effect of geomorphological change on the spatial variability of the precision of SfM-MVS 3D point-cloud models. AUC Geographica 61(1), 3–15
https://doi.org/10.14712/23361980.2025.6

1. Introduction

Within a decade or so (Fonstad et al. 2013; Gomez 2012, 2013; James and Robson 2012; Westoby et al. 2012), SfM-MVS (Structure from Motion – Multiple View Stereophotogrammetry) has deeply transformed the fields of geo-sciences interested in constructing "precise objects' morphology" for a "low-cost", as it offers high spatial density measurement for potentially extensive areas.

The SfM-MVS method enables the reconstruction of three-dimensional spatial models from a series of overlapping two-dimensional images (Szeliski 2010). This technique has been widely applied to various fields outside geosciences as well: e.g. archaeology (de Reu et al. 2013, 2014; Verhoeven 2011), terrain surveying, and robotic navigation (Hixon et al. 2018; Deliry and Avdan 2021; Saputra et al. 2018). In combination with the rapid advancement of Unmanned Aerial Vehicle (UAV) technology, SfM-MVS has been particularly instrumental in geosciences for the production of DEMs (Digital Elevation Models) and DSMs (Digital Surface Models). Furthermore, UAVs also allow the access to previously difficult or unreachable areas (e.g. Gomez 2023; Hayakawa et al. 2020). Consequently, SfM-MVS has been applied to a wide range of environment from the bottom of the ocean to the mountain tops: submarine morphology (Lockhead and Hedley 2022; Qiao et al. 2019), coastal morphology (e.g. Clark et al. 2021; Gomez et al. 2023; Hayakawa et al. 2020), floodplain analysis (e.g. Bakker et al. 2017), mountainous terrains (e.g. Bi et al. 2023), and volcanic landscapes (Gomez 2014; Gomez et al. 2022), including the reconstruction of vegetation and trees (Morgenstern and Gomez 2014).

Because of its low cost and versatility, the method has also been extensively employed to depict topographic variations over time, in order to quantify fast-evolving landscapes. Among other examples, SfM-MVS has been particularly useful to quantify the dynamic of mountain landslides (Mauri et al. 2021; Peppa et al. 2018) and coastal landslides (Esposito et al. 2017), coastal dunes' erosion and deposition (Mestre-Runge et al. 2023), as well as gully erosion and deposition where seasonal to yearly change are important (Tsunetaka et al. 2021; Gomez et al. 2021). The comparisons between the different time-steps are either been done at the pointcloud level (Lague et al. 2013; Esposito et al. 2017) or at the DEM level (e.g. Mauri et al. 2021), using vertical matching of the data.

To work across spatial scales and repeated surveys, error analysis is essential, and so is the georeferencing against ground control points (GCPs), especially for repeated surveys (Forlani et al. 2018). But, even with GCPs' constraints, Liu et al. (2022) noted a variability in the produced point-clouds even under identical conditions. One of the challenges is due to the multiple sources of error. It includes influences from the terrain itself, inaccuracies due to the camera or the lens characteristics, as well as computational errors (Westoby et al. 2012; Deliry et al. 2021). Notably, many studies tend to investigate error as a bundled dataset, while there is still a need to separate the influence of different parameters on the error. This is of particular importance, because the use of SfM-MVS is often motivated by its potential high-precision (Iheaturu et al. 2020; Panagiotidis et al. 2016). Accordingly, geoscientists have developed several methods to test the precision of different models, notably with the increased use of UAVs for DEMs' construction (Tab. 1).

Tab. 1 Accuracy Evaluation Studies in UAV Photogrammetry and SfM.

Environment	Evaluation Criteria	Error or Conclusion	Reference
Sandy coastal topography via UAV	Vertical accuracy, compared with GCPs	0.09–0.11 m	Long et al. (2016)
Riverbed topography	Mean error/standard deviation, compared with GCPs	0.016–0.089 m / 0.065–0.085	Woodget et al. (2015)
Snow depth RMSEs	RMSE of depth of snow on rocks/grass, compared to manual probe measurements	0.07–0.15 m / 0.3m	Bühler et al. ; Gindraux et al. (2016/2017)
Landslide monitoring RMSEs with UAVs	Horizontal/vertical RMSE compared with GCPs	0.07 m, 0.06 m	Lucieer et al. (2014)
Terrain models in moraines (UAV)	RMSE, compared with GCPs	0.2 m, 0.59 m in dense vegetation	Tonkin et al. (2014)
UAV-SFM accuracy test in flat areas	MSE in X, Y and Z coordinates, compared with GCPs	20.93 mm, 18.48 mm and 46.05 mm	Iheaturu et al. (2020)
UAV-SfM in fluvial channels	Sediment volume estimation, compared with terrestrial laser scanning	Effective for sediment changes	Tsunetaka et al. (2020)
UAS-SfM accuracy vs traditional methods	Factors impacting UAS-SfM accuracy	Accuracy mainly depends on sensor resolution, flight height, image overlaps, and the number, distribution, and accuracy of GCPs	Deliry et al. (2021)
Accuracy of UAV-SFM on farmland with vegetation	Vertical RMSE, compared with GCPs	approximately 10cm	Peppa et al. (2016)

Despite these advances, the inherent error due to the repeat of topographic modelling using SfM-MVS still needs further research (Zhao et al. 2021).

Therefore, out of a broad set of potential issues (lighting, seasonality, reflectance and color of the target, position of the camera, etc.), in this contribution the authors propose to investigate (1) the variability among repeats and (2) the role of topographic variation on the error generated by repeats, notably because the spatial error propagation is a well-known phenomenon in photogrammetry, which is arguably affecting the results of multiple SfM-MVS models.

2. Methodology

The authors propose to reach the goal mentioned above, by using a controlled environment (single-color sand, controlled lighting) in order to derive a model of precision (the accuracy component of the error is difficult to reach, as for most SfM-MVS models in geomorphology, because the real shape measured is not perfectly known), as for complex targets found in the natural environment, it is difficult to define a benchmark measure of object, and error can be approached from the variability of precision between the repetition of the same measure.

The methodology of the present contribution is based on the repeated SfM-MVS measurements (Fig. 1) of an unvarying surface based on the following experimental procedure, to which two generations of sand mount were added to produce three generations of experiments.

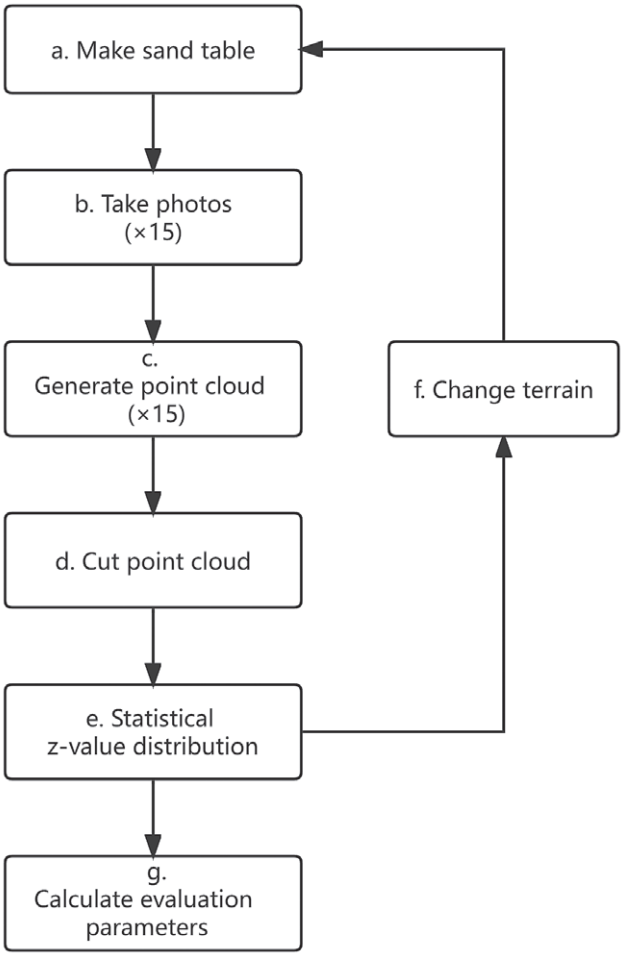

Fig. 1 Point cloud generation and analysis process.

2.1 Material, data acquisition and 3D model construction

For the present research, a sandbox model was crafted using acrylic plates and double-sided tape on which a single layer of calibrated 0.5 mm yellow color silicates covers the surface. This allows the experimental setup to have a regular roughness and surface height. The experiments include (a) one set of experiments using the flat surface, then (b) a set of experiments with a conical mount made of 50 ml of sand poured in the center of the experimental model, and finally (c) a set of experiments with a sand cone of 100 ml in the centre. Each set of experiments is made of 15 repetitions of the same measure, and each of the 15 repetitions was captured using 45 to 50 photographs using a Ricoh camera (Tab. 2).

Each set of photographs was then processed using the SfM-MVS algorithm in Metashape-Pro® (Agisoft©) to generate the point cloud data (e.g. Tinkham et al. 2021; Catala-Roman et al. 2024). The processing started from a sparse point-cloud reconstruction and then a dense point-cloud reconstruction, and the registration of the pointcloud was done using the targets that can be automatically recognized (cf. Tab. 3).

Tab. 2 The equipment and software used in the experiment.

Sand Table	Base	Acrylic Board + Double-sided Tape	
	Sand	0～100 ml Yellow Sand	
GCP	18 Marks from Metashape		
Camera	Main Body	RICOH WG-7	
	Lens	RICOH DW-5 171930*	
	Pixel	5184 × 3888	
Computer	DELL G15 5520	CPU	12th Gen Intel(R) Core(TM)i7-12700H 2.30Ghz
		GPU	NVIDIA GeForce RTX 3060 Laptop 8G
		RAM	16GB 4800Mhz
Soft	Generate Point Cloud	Metashape	
	Processing	Python	
Camera Position	Shooting height	45 ± 3cm	
	Tilt	< 10% taken as Nadir	

* Additional lenses to eliminate distortion caused by camera lenses (Wang et al. 2008; Wang et al. 2022).

Tab. 3 Examples of point clouds generated from different volumes of sand.

Sand volume	Top view	Tilt view
0 ml	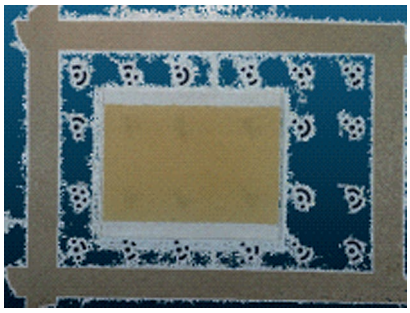	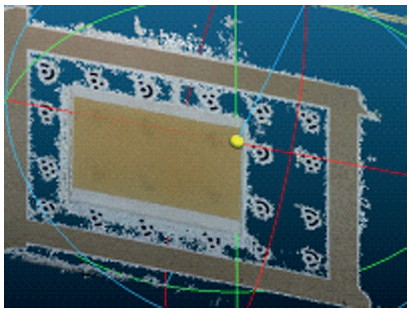
50 ml	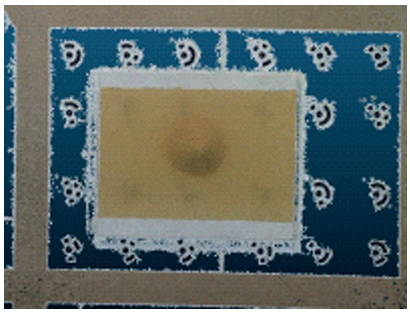	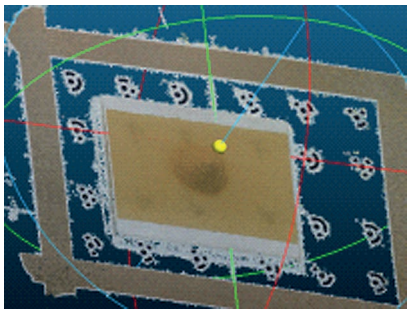
100 ml	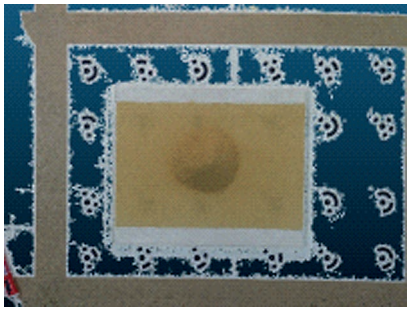	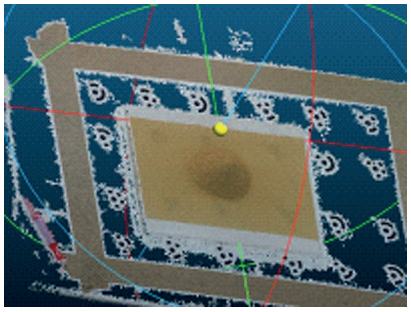

After cropping all the points outside the experimental table covered with yellow sand, the number of points generated for each experiment is on average ~800,000 points, with a maximum of 1,012,235 points and a minimum of 710,705 points generated for the experiments using the flat surface only. For the experiments with a sand cone of 50ml, the number of points is on average of 930,000 points, with a maximum of 1,139,308 points and a minimum of 794,791 points. Finally, the pointclouds for the experiments with the 100 ml sand cone displays an average points' numbers of 1,000,000 points, with a maximum of 1,265,351 points and a minimum of 874,874 points.

2.2 Data Analysis and statistical simulation

Subsequently, Python was employed to segment the point cloud data, perform counts, and compute the different statistical parameters to assess variability. For this purpose, the point cloud data was then divided into a 5 × 8 grid cells, so that the Z-values in each grid cell was handled as statistical populations, for which distribution functions were created to compare the different locations on the cell (Fig. 2).

Then for each grid cell, the authors calculated distribution of the Z-value and determine the distribution function using the distribution peak and its

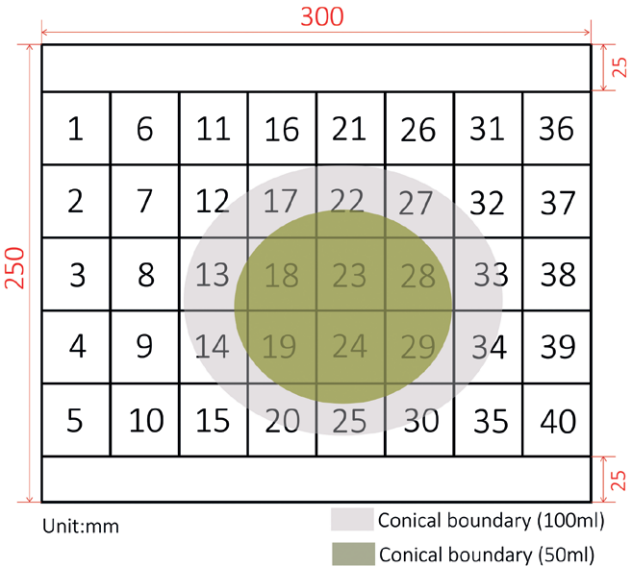

Fig. 2 Grid cells division of sand table (in the result section, the cell number refer to the numbers in this table).

position (peak-z), the left and right tails (labelled Min-z and Max-z), the full width at half-maximum (FWHM), and the interquartile spacing (IQR). The distribution of the Z-values was then computed using the Gaussian Kernel Density Estimation (KDE) method (Zaman et al. 2017). KDE is a non-parametric method employed for estimating the Probability Density Functions (PDF):

$$\hat{f}(x) = \frac{1}{nh}\sum_{i=1}^{n} K\left(\frac{x-x_i}{h}\right) \quad (1)$$

where $\hat{f}(x)$ represents the estimated density at point x, and $x_1, x_2, \ldots, x_n$ are the sample points, K is the kernel function, and is the bandwidth. This method has been used to analyze the spatial distribution characteristics of point cloud data for 3D modeling, 3D object recognition, and 3D model registration (Zhang et al. 2021), especially when datasets have varying resolutions and qualities (King et al. 2016; Vestal et al. 2021), which was estimated to be one of the working assumption for the present study as the average number of points varied between the different types of experiments.

Because the objective of the present study is to investigate the spatial variability of the error in seemingly unchanging surface, the distribution function of each grid-cell was analysed separately. To provide a synthetic view of the points, the peak horizontal coordinate (Peak-z), the minimum Z-value (Min-z), the maximum Z-value (Max-z), the Full Width at Half Maximum (FWHM), and the Interquartile Range (IQR) were used as statistical markers (cf. summary Tab. 4).

Tab. 4 Evaluation parameters.

Parameter	Calculation Method	Remarks
Peak-z	–	The horizontal coordinate of the vertex in the z-value distribution function.
Min-z	–	Represents the lowest value in the distribution, indicating the lower limit of Z-values.
Max-z	–	Represents the highest value in the distribution, indicating the upper limit of Z-values.
FWHM	$FWHM = x_r - x_l$	Describes the width of the distribution defined as the width at which the function value reaches half of its maximum value. Here x_r, x_l, are the horizontal coordinates on the distribution curve where the function value reaches half of the maximum on the right and left sides, respectively.
IQR	$IQR = Q_3 - Q_1$	A statistical measure describing the dispersion of a distribution representing the range of the middle 50% of the data. Where Q_3 is the third quartile (75th percentile), and Q_1 is the first quartile (25th percentile).

3. Results

Using the same acquisition method on the same surface several times is showing an expected variability in the elevation. Furthermore, on a seamlessly homogeneous surface, this variability shows spatial dependence. The results of the experiments show the greatest variations for experiments Y0-1 to Y0-15 using the flat 10 mm thick plate (Tab. 5), the peak values of Z ranged over 0.117 mm, averaging between 10.84 mm and 10.96 mm, with the greatest difference observed in grid cell 1 (detailed results for each cell of each experiment are provided in the appendix).The difference in the maximum values varied between 0.072 mm and 0.341 mm in 15 replicates. The difference in Min-z values ranged from 0.068 mm to 0.206 mm, with an outlier value of 9.627 mm in grid cell 21 removed, and the average min-z value for the same grid cell was 10.574. The Max-z values ranged between 10.813 mm and 11.154 mm, with grid cell 35 showing the greatest variation. FWHM values extended from 0.19 to 0.286, and grid cell 27 displayed the largest variability. The IQR spanned from 0.102 to 0.148, with grid cell 27 also exhibiting the most distinct differences. The extent of variability across these measurements is evidence in the statistical indicators of Peak-z, Min-z, Max-z, FWHM, and IQR (Tab. 5).

For the experiments where the surface is "flat", the changes of Peak-z, FWHM and IQR were not significant. (Tab. 5). However, within each experiment, the variability of the minimum and maximum value can vary by about 10% (e.g. Y0-8 in Tab. 5).

Tab. 5 Z-value distribution of point cloud with the cells where the largest variability was observed for the flat environment (i.e. no extra-sand added).

	Peak-z	Min-z	Max-z	FWHM	IQR
	Cell-1	Cell-21	Cell-35	Cell-27	Cell-27
Y0-1	10.848	10.584	10.970	0.190	0.102
Y0-2	10.933	10.601	10.892	0.227	0.122
Y0-3	10.964	10.565	10.842	0.239	0.126
Y0-4	10.897	10.544	10.904	0.230	0.119
Y0-5	10.923	10.571	10.935	0.215	0.114
Y0-6	10.940	10.525	10.813	0.238	0.128
Y0-7	10.919	10.490	10.876	0.237	0.126
Y0-8	10.939	9.627	11.154	0.238	0.125
Y0-9	10.953	10.635	10.834	0.217	0.115
Y0-10	10.936	10.617	10.978	0.200	0.109
Y0-11	10.921	10.646	10.885	0.254	0.131
Y0-12	10.915	10.603	11.061	0.264	0.138
Y0-13	10.919	10.542	10.952	0.286	0.148
Y0-14	10.893	10.577	10.957	0.231	0.119
Y0-15	10.916	10.530	10.895	0.227	0.120
Difference	0.117	1.019	0.341	0.096	0.047

Overall, the precision is decreasing when the topography becomes more complex (i.e. with the central conic pile of sand). For the scenario where 50 ml of sand was added, the Peak-z values for Y50-1 to Y50-15 ranged from 18.783 to 19.494, with grid cell-1 showing the most significant differences. Min-z values oscillated between 10.094 and 10.673, with the largest variations in grid cell-36. Max-z exhibited a range from 18.553 to 18.833, with grid cell-35 displaying the most noticeable variability. FWHM varied from 12.411 to 12.950, with grid cell-27 having the most pronounced differences. The IQR extended from 7.063 to 7.223, with the greatest variability again observed in grid cell-27. These data points highlight the impact of added sand on the variability of the measurements (Tab. 6).

The second set of experiments revealed a significant increase in the variability of the SfM method, particularly in the Peak-z parameter, which exhibited the most notable variability. The Peak-z variability substantially increased, showing a deviation of 0.711 mm. This heightened variability may be attributed to changes in the surface morphology of the sandbox, resulting in greater uncertainty in the SfM method when measuring similar features. While the variability in FWHM and IQR is lower compared to the experiments without added sand, it still shows some increase. Furthermore, the variability of Min-Z increased, but the variability of Max-Z decreased slightly. In this scenario, a change in the Peak-z of the distribution function is observed, while the shape of the curve displays smaller variations.

Upon adding 100 ml of sand (Tab. 7), the dataset (Y100-1 to Y100-15) showed Peak-z values ranging from 22.959 to 23.451, with grid cell-1 exhibiting the most variability. Min-z ranged from 10.495 to 10.727, with the most significant differences in grid cell-36. Max-z values varied between 19.305 and 19.628, with grid cell-35 showing the greatest range of variability. FWHM was observed to range from 16.870 to 17.351, with the largest differences in grid cell-27. The IQR varied from 5.472 to 5.619, with the most variability again noted in grid cell-27.

With the addition of 100 ml of sand, the variability in Peak-z remains relatively high but is reduced compared to the 50 ml sand addition. Despite the increased volume of sand, the complexity of the surface shape does not increase correspondingly. This may suggest that the SfM method can achieve more stable results for larger targets. The continued low variability in FWHM and IQR also indicates that the shape of the distribution function undergoes minimal change.

Even for the grid cells that do not display any significant change, the variability of the Z values is changing in between experiments. The presence of the 50 ml and then 100 ml sand cone is impacting the variability of grid cells where the sand cone is not located (Fig. 3). The cells the further away from the cone are grid cells cell-1, cell-5, cell-36 and cell-40, and the spread of the z-values as well as the position (mean, minimum and maximum) are all changing significantly (Fig. 3). The peak value of cell 1 first increases and then decreases, from experiments Y0 to Y50 to Y100, while the spread of the measurements decreases. The peak position of

Tab. 6 Z-value distribution of point cloud and the cell of the largest difference: 50 ml.

	Peak-z	Min-z	Max-z	FWHM	IQR
	Cell-29	Cell-6	Cell-20	Cell-28	Cell-25
Y50-1	19.110	10.614	18.741	12.411	7.134
Y50-2	19.144	10.647	18.754	12.606	7.223
Y50-3	19.072	10.591	18.697	12.579	7.117
Y50-4	18.945	10.630	18.742	12.508	7.075
Y50-5	19.131	10.094	18.685	12.602	7.161
Y50-6	19.343	10.612	18.661	12.728	7.063
Y50-7	19.037	10.629	18.833	12.617	7.145
Y50-8	19.126	10.550	18.751	12.570	7.139
Y50-9	19.022	10.545	18.726	12.577	7.170
Y50-10	19.494	10.576	18.565	12.950	7.139
Y50-11	19.437	10.673	18.715	12.641	7.163
Y50-12	19.012	10.601	18.704	12.681	7.185
Y50-13	19.339	10.576	18.684	12.698	7.159
Y50-14	19.228	10.439	18.553	12.813	7.141
Y50-15	18.783	10.526	18.671	12.571	7.119
Difference	0.711	0.578	0.280	0.539	0.160

Tab. 7 Z-value distribution of point cloud and the cell of the largest difference: 100 ml.

	Peak-z	Min-z	Max-z	FWHM	IQR
	Cell-19	Cell-37	Cell-27	Cell-18	Cell-20
Y100-1	23.257	10.677	19.383	16.870	5.530
Y100-2	22.959	10.624	19.420	17.189	5.502
Y100-3	23.152	10.575	19.461	16.874	5.501
Y100-4	23.159	10.643	19.445	16.992	5.543
Y100-5	23.168	10.603	19.511	17.084	5.577
Y100-6	23.084	10.495	19.305	16.904	5.503
Y100-7	23.327	10.590	19.476	17.351	5.576
Y100-8	23.110	10.637	19.373	16.867	5.483
Y100-9	23.114	10.645	19.583	16.935	5.486
Y100-10	23.092	10.685	19.463	17.037	5.552
Y100-11	23.034	10.623	19.440	17.019	5.524
Y100-12	23.451	10.641	19.495	17.283	5.472
Y100-13	23.097	10.625	19.417	17.032	5.541
Y100-14	23.230	10.727	19.628	17.099	5.524
Y100-15	23.105	10.632	19.437	17.142	5.619
Difference	0.492	0.232	0.322	0.484	0.147

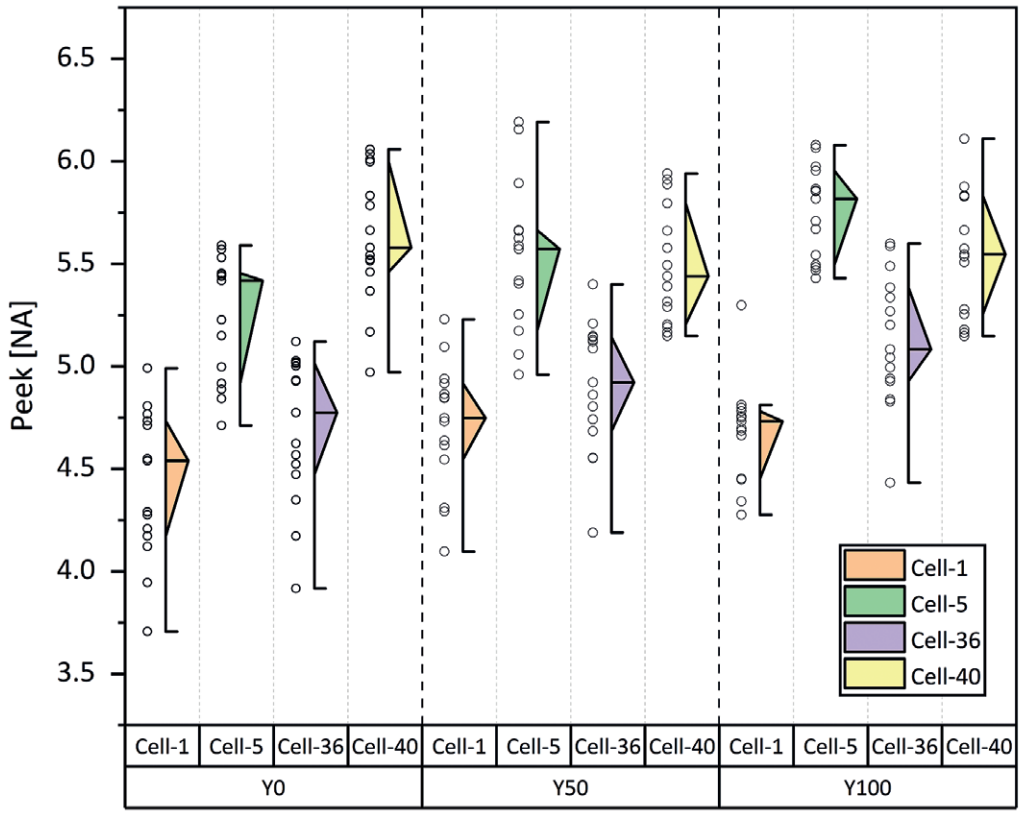

Fig. 3 Spatial Variability of the Z-Peak Values. The magnitude of the peak indicates the concentration of the data. The variation in the width of the peak distribution indicates changes in variability. Significant differences are observed even in areas without topographical changes, such as in Cell-1 and Cell-5. Furthermore, these variations exhibit different trends at different locations.

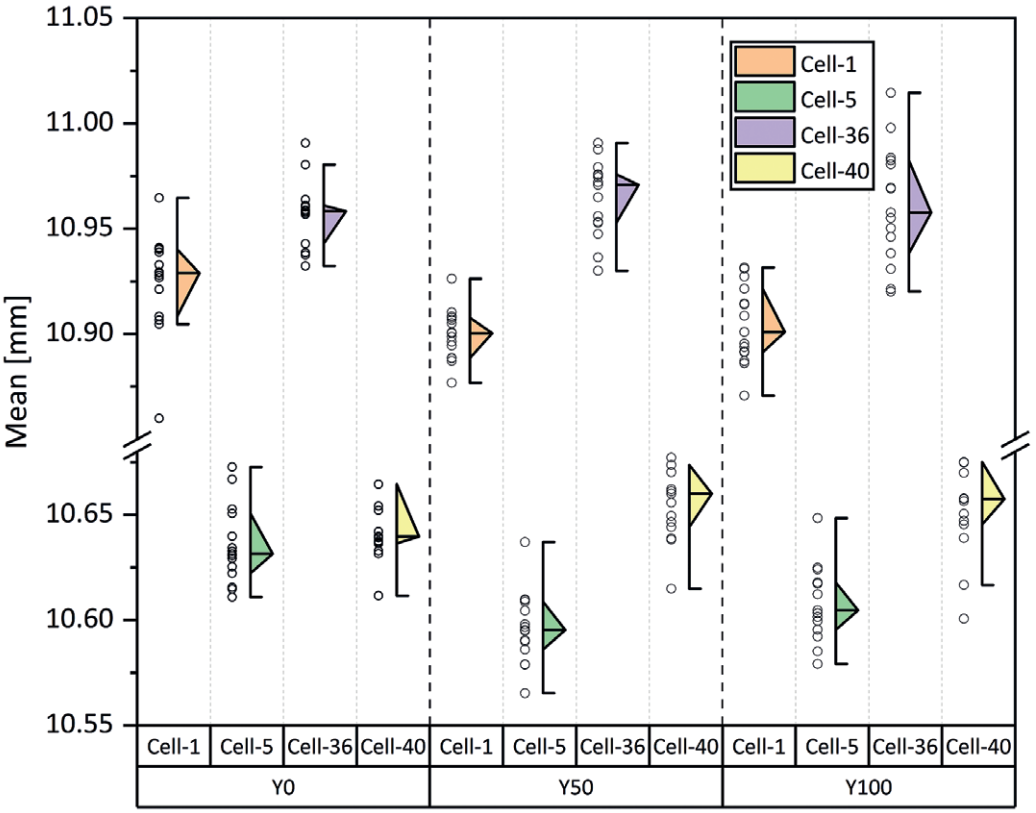

Fig. 4 Spatial Variability of Distribution Mean Values of Z. Variations in the mean suggest that the overall cell is influenced by topographical changes. Fluctuations are significant at various locations, with the changes in Cell-36 being particularly notable, demonstrating higher instability.

cell-5 increases, and the dispersion first increases and then decreases. The peak value of grid 36 is larger, but the dispersion is basically unchanged. Finally, the peak of the cell 40 grid decreases slightly and instead becomes more dispersed (Fig. 3).

For the same cell, the mean fluctuates somewhat, but the degree of dispersion is basically the same (Fig. 4). The mean decreased in Cell-1, and slightly increased in Cell-5 in Y-100, and their degree of dispersion remained basically unchanged. Cell-40 is stable, but the dispersion of Cell-36 increases significantly.

When the spatial distribution and repeated measurements are displayed together, the differences between cells can be significantly observed. Calculate the standard deviation of the remaining cells after removing the area that the sand will cover. In Fig. 5-a, cell-1, cell-2, and cell-6 show large standard deviations, and several positions in the 8th measurement show large standard deviations. After the addition of 50 ml sand, the standard deviation of each cell decreased, but cell-1 and cell-2 were still significantly higher than other positions (Fig. 5-b). When 100 ml of sand was added, higher standard deviations were observed for cell-1, cell-2, and cell-26 (Fig. 5-c). In general, the change of terrain does lead to different degrees of variation in the standard deviation of each location. From this representation of the data, one can see that the standard deviation of the points in each cell can vary, and so within a single set of experiments, with two corner locations showing consistently the highest standard deviation. Moreover, the increased in standard deviation does not seem to be related to the repeats themselves, as the variability is moving in space rather than just in between repeats.

4. Discussion

4.1 Summary of the main findings

In the present contribution, the authors have added to the already known issue of error in SfM-MVS measurement of the land surface a spatial dimension, showing that the error can be location dependent. This finding is consistent with previous studies that have reported spatial variability in SfM-MVS accuracy (James and Robson 2012; Fonstad et al. 2013; Smith and Vericat 2015). Furthermore, the steeper the terrain, the larger the error. This phenomenon is already notably known, with problems such as doming effects and increase of the topographic maxima (James and Robson 2014; Javernick et al. 2014; Eltner et al. 2016). However, the novelty of the present contribution shows that flat surfaces close to areas with high topographic variability also experience an increased error. In previous work, Gomez et al. (2015) found that the SfM measurement over forested canopy was in the range of 10 m at the landscape scale, but the author did not consider the spatial diffusion of this error to other areas, and it is most likely that this error diffused in other areas, as a function of the elevation variability as shown in the present results.

4.2 Importance of the results for repeated measurements

This "tele-connection" of surrounding features on the error on "flat surfaces" is particularly important for research involving the repetition of measurements over time, in order to measure land deformation (Cucchiaro et al. 2020; Hemmelder et al. 2021). Indeed, it cannot be expected that the error will remain the same at a control point, event if it is known to be stable as long as other parts of the landscape are changing. It is thus important to reconsider this point for the measure of for instance: from coastal erosion (e.g. Fabris et al. 2021; Terefenko et al. 2018) and coastal sand-dune evolution (e.g. Gomez et al. 2024) to the evolution of volcanic gullies at mid- (e.g. Tsunetaka et al. 2021) to longer-term (e.g. Gomez et al. 2014), including the built-environment (e.g. Wei et al. 2021 for urban surface displacement). This observation can be further extended when surveying is conducted at different periods of the years (e.g. Micheletti et al. 2015; Groos et al. 2019; Niederheiser et al. 2021), as the vegetation growth and geometry change will modify the whole geometry of the scene.

4.3 Error "tele-connection" and surrounding morphology

The present experimental work has been investigating the variability in measured vertical values (topography for instance), using a regular flat surface, made of only one grain-size and one color, and two other surfaces with a central sand cone. As expected, the error varies from one repeat to another almost randomly, but the most important result is the "tele-connection" of the error when a spatially disconnected morphology change. In other words, surrounding geometries can influence a surrounding flat surface. In term of geomorphology a volcanic structure growing, or a landslide moving over a terrain has the potential to modify the error at target locations that are not subject to movement or any change.

Similar observations were made by Dr. Tsunetaka when he was preparing one of manuscript on Unzen Volcano (Tsunetaka et al. 2021). He stated that Ground Control Points were leading to different spatial spread of the error depending on the position of the Ground Control Point, especially in relation with the surrounding topography (private communication). In other words, topographic variability in the vicinity of one or a set of control points can lead to a change in the error at the control points, showing a similar "teleconnection" between surrounding features and the points on a flat area.

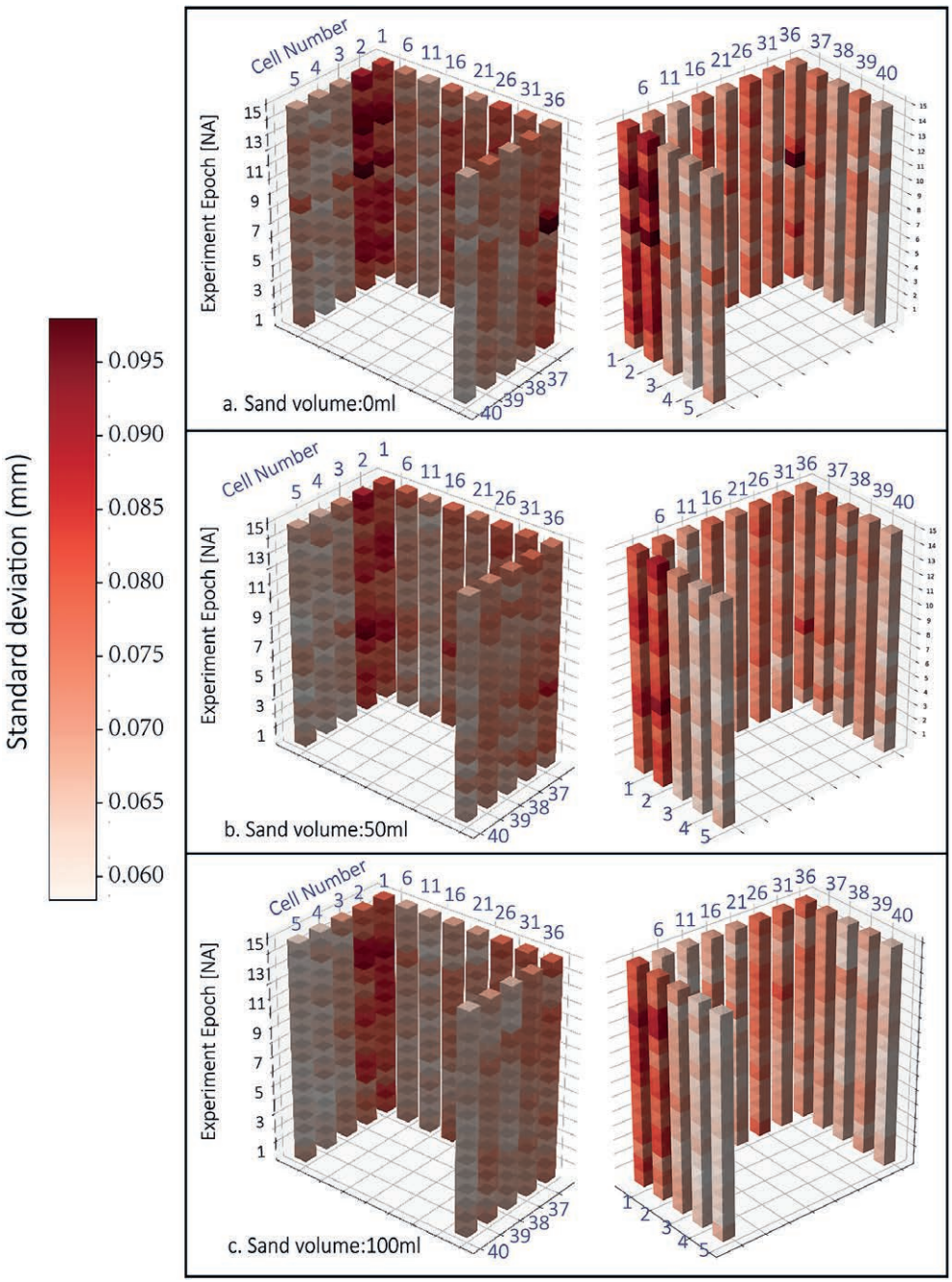

Fig. 5 Spatial Variability of the altitude (Z) standard deviation; (a) no extra sand, (b) 50 ml of sand added, and (c) 100 ml of sand added. The cells used for comparison are the one on the periphery of the experimental box, where no topographic change occurred over all the experiments. Each repeat of the experiment is displayed as a vertical level. The views on the left and right for each experiments a, b and c show the data from a different angle for easier reading.

4.4 Comparison with Geomorphological structures

In order to apply the error analysis to the actual terrain, based on the experimental results of this study, the error index is calculated according to formula 2.

$$E_h = \frac{Z_{max} - Z_{min}}{h} \times 100\% \quad (2)$$

Where E_h is the range of elevation fluctuation. Z_{max} and Z_{min} are the maximum and minimum values of the average elevation of the midpoint in the grid cell, respectively. is the average elevation of the grid cell. The calculation results are shown in the Tab. 8, and there is the lowest elevation without adding sand, that is, the thickness of the acrylic sheet, which is about 10.723 mm. The variability error at this point is about 0.431% to 0.959%. After adding 50 ml of sand, the elevation reaches about 29.868 mm, and the error decreases, ranging from 0.312 to 0.763%. After adding 100 ml of sand, the elevation is 37.535 mm, and the error range becomes larger at this time, rising to 0.256~1.226%.

Tab. 8 Relationship between height and error range.

Sand volume (ml)	Height of sand table (mm)	Error range
0	≈ 10.723	0.431~0.959%
50	≈ 29.868	0.312~0.763%
100	≈ 37.535	0.256~1.226%

For flat cells that do not undergo topographic changes throughout, their variability will also be affected by changes in the central topography. In the absence of additional sand, the variability in these areas ranges from 0.0058 to 0.1047 mm, with a mean of 0.075 (e.g. Fig. 6). When the microtopography of the central area fluctuates, the variability decreases significantly, ranging from 0.0421 to 0.0719, and the variability becomes relatively evenly distributed, concentrated around the average value of 0.0609 (e.g. Fig. 6). Considering the micro-topography with a 100 ml of sand, the measured vertical variability increaed, with variability ranging from 0.0608 and 0.1333. The change range was far greater than the previous two cases (e.g. Fig. 6). This suggests that even in areas where no terrain change has occurred, the error will be affected by the surrounding terrain. However, the error range measured in the present set of experiments is inferior to the grain-size height (0.5 mm) by almost a factor of 5, even for the highest recorded values. As the authors have used a rigid acrylic sheet, which can be taken as perfectly flat, the total error of the model can be represented as a combination of the measured precision (0.1333 mm) and the variability induced by the particles over the acrylic sheet (with values between 0 and 0.5 mm, or half the particle height if one only considers the upper half of the particles).

4.5 Comparison with error arising from topographic change

Common sources of error linked to topographic change when using SfM-MVS are linked to at least four important sources: (1) perspective distortion: Steep topography can cause perspective distortion in the captured images. This distortion affects the accuracy of the feature matching and triangulation processes in SfM. The perspective projection equation, which relates 3D world coordinates to 2D image coordinates, is sensitive to large depth variations (Hartley and Zisserman 2004); (2) depth uncertainty: In areas of steep topographic changes, the depth estimation from triangulation becomes less reliable, because the depth uncertainty is inversely proportional to the baseline (distance between camera positions) and directly proportional to the depth (Gallup et al. 2007). Steep surfaces often have larger depths relative to the baseline, leading to higher depth uncertainty; from 1 and 2, then (3) occlusions and visibility will increase the error (e.g. Furukawa and Ponce 2010). Finally, (4), steep topographic changes can make it challenging

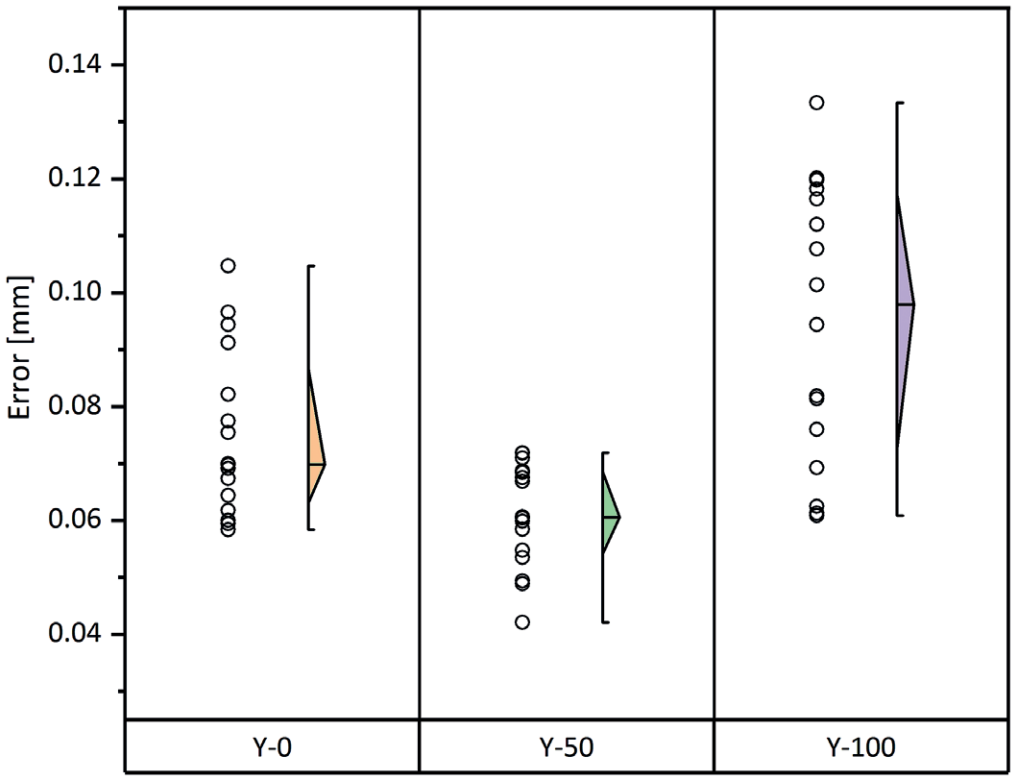

Fig. 6 Changes in flat cell variability. The error range < sand grain-size, potentially suggesting that maximum grain-size on an outdoor surface may be a good indicator of precision variability under similar conditions.

to accurately estimate surface normals, as the local neighborhood around a point may have significant depth variations (Kazhdan and Hoppe 2013). In the present case however, the topographic change are all resulting from a regular dome-shaped controlled by the sand internal-friction angle, and the source of variability is thus different, however the increased error at the corners (Fig. 5) may be related to a difficulty to estimate the normal, due to the immediate location at the edge of the acrylic sheet, but it remains insufficient in explaining the variability between the different types of experiments.

The present contribution confirms the recognized diffusion of error across a measured scene, but it newly demonstrates that the "tele-connection" of errors are driven by the topographic variability, and that repeated measurements need to be considered in order to address inherent error due to measurements. It also demonstrates that the relation between topographic height and variability in the recorded values is not linear, and according to the existing literature on steep slopes and SfM-MVS error, the error is likely to increase with the slope of the topographic feature. Interestingly, the experiments were all conducted with the same lighting and homogeneous single color sand surface, but yet spatial variability in the error was also apparent showing the need to mitigate both precision problems linked to the method and the target (as three sets of vertical variability were tested). This is particularly important when attempting to measure erosion and other surface changes over time, and the variability observed in the present set of experiments may be exacerbated or multiplied under the influence of other factors.

References

Bakker, M., Lane, S. N. (2017): Archival photogrammetric analysis of river-floodplain systems using Structure from Motion (SfM) methods. Earth Surface Processes and Landforms 42(8), 1274–1286, https://doi.org/10.1002/esp.4085.

Bi, R., Gan, S., Yuan, X., Li, R., Gao, S., Yang, M., Luo, W., Hu, L. (2023): Multi-View Analysis of High-Resolution Geomorphic Features in Complex Mountains Based on UAV–LiDAR and SfM–MVS: A Case Study of the Northern Pit Rim Structure of the Mountains of Lufeng, China. Applied Sciences 13(2): 738, https://doi.org/10.3390/app13020738.

Bühler, Y., Adams, M. S., Bösch, R., Stoffel, A. (2016): Mapping snow depth in alpine terrain with unmanned aerial systems (UASs): potential and limitations. Cryosphere 10(3), 1075–1088, https://doi.org/10.5194/tc-10-1075-2016.

Clark, A., Moorman, B., Whalen, D., Fraser, P. (2021): Arctic coastal erosion: UAV-SfM data collection strategies for planimetric and volumetric measurements. Arctic Science 7(3), 605–633, https://doi.org/10.1139/as-2020-0021.

Cucchiaro, S., Maset, E., Cavalli, M., Crema, S., Marchi, L., Beinat, A., Cazorzi, F. (2020): How does co-registration affect geomorphic change estimates in multi-temporal surveys? GIScience and Remote Sensing 57(5), 611–632, https://doi.org/10.1080/15481603.2020.1763048.

De Reu, J., De Smedt, P., Herremans, D., Van Meirvenne, M., Laloo, P., De Clercq, W. (2014): On introducing an image-based 3D reconstruction method in archaeological excavation practice. Journal of Archaeological Science 41, 251–262, https://doi.org/10.1016/j.jas.2013.08.020.

De Reu, J., Plets, G., Verhoeven, G., De Smedt, P., Bats, M., Cherretté, B., De Maeyer, W., Deconynck, J., Herremans, D., Laloo, P., Van Meirvenne, M., De Clercq, W. (2013): Towards a three-dimensional cost-effective registration of the archaeological heritage. Journal of Archaeological Science 40(2), 1108–1121, https://doi.org/10.1016/j.jas.2012.08.040.

Deliry, S. I., Avdan, U. (2021): Accuracy of unmanned aerial systems photogrammetry and structure from motion in surveying and mapping: a review. Journal of the Indian Society of Remote Sensing 49(8), 1997–2017, https://doi.org/10.1007/s12524-021-01366-x.

Eckert-Gallup, A., Martin, N. (2016): Kernel density estimation (KDE) with adaptive bandwidth selection for environmental contours of extreme sea states. OCEANS 2016 MTS/IEEE Monterey, CA, USA, 1–5, https://doi.org/10.1109/OCEANS.2016.7761150.

Eltner, A., Kaiser, A., Castillo, C., Rock, G., Neugirg, F., Abellán, A. (2016): Image-based surface reconstruction in geomorphometry – merits, limits and developments. Earth Surface Dynamics 4(2), 359–389, https://doi.org/10.5194/esurf-4-359-2016.

Fabris, M. (2021): Monitoring the coastal changes of the Po River delta (Northern Italy) since 1911 using archival cartography, multi-temporal aerial photogrammetry and LiDAR data: Implications for coastline changes in 2100 AD. Remote Sensing 13(3): 529, https://doi.org/10.3390/rs13030529.

Fonstad, M. A., Dietrich, J. T., Courville, B. C., Jensen, J. L., Carbonneau, P. E. (2013): Topographic structure from motion: a new development in photogrammetric measurement. Earth Surface Processes and Landforms 38(4), 421–430, https://doi.org/10.1002/esp.3366.

Furukawa, Y., Ponce, J. (2009): Accurate, dense, and robust multiview stereopsis. IEEE Transactions on Pattern Analysis and Machine Intelligence 32(8), 1362–1376, https://doi.org/10.1109/TPAMI.2009.161.

Gallup, D., Frahm, J. M., Mordohai, P., Yang, Q., Pollefeys, M. (2007): Real-time plane-sweeping stereo with multiple sweeping directions. In 2007 IEEE Conference on Computer Vision and Pattern Recognition, Minneapolis, MN, USA, 1–8, https://doi.org/10.1109/CVPR.2007.383245.

Gomez, C. (2012): Historical 3D topographic reconstruction of the Iwaki Volcano using structure from motion from uncalibrated aerial photographs. HAL science ouverte: hal-00765723, version 1. Available online: https://hal.archives-ouvertes.fr/hal-00765723 (accessed on 5. 1. 2024).

Gomez, C. (2014): Digital photogrammetry and GIS-based analysis of the bio-geomorphological evolution of Sakurajima Volcano, diachronic analysis from 1947 to 2006. Journal of Volcanology and Geothermal 280, 1–13, https://doi.org/10.1016/j.jvolgeores.2014.04.015.

Gomez, C. (2022): Point Cloud Technologies for Geomorphologists: From Data Acquisition to Processing. Springer Nature, Switzerland.

Gomez, C., Hayakawa, Y., Obanawa, H. (2015): A study of Japanese landscapes using structure from motion derived DSMs and DEMs based on historical aerial photographs: New opportunities for vegetation monitoring and diachronic geomorphology. Geomorphology 242, 11–20, https://doi.org/10.1016/j.geomorph.2015.02.021.

Gomez, C., Liu, J., Wu, J., Persendt, F., Bradak, B., Saleh, Y., Hadmoko, D. S. (2023): Improving vegetation spatial distribution mapping in arid and on coastal dune systems using GPR in Tottori Prefecture (Japan). AUC Geographica 58(2), 238–249, https://doi.org/10.14712/23361980.2023.18.

Gomez, C., Setiawan, M. A., Listyaningrum, N., Wibowo, S. B., Hadmoko, D. S., Suryanto, W., Darmawan, H., Bradak, B., Daikai, R., Sunardi, S., Prasetyo, Y., Astari, A. J., Lukman, L., Nurani, I. W., Dede, M., Suhendro, I., Lavigne, F., Malawani, M. N. (2022): LiDAR and UAV SfM-MVS of Merapi volcanic dome and crater rim change from 2012 to 2014. Remote Sensing 14(20): 5193, https://doi.org/10.3390/rs14205193.

Gomez, C., Shinohara, Y., Tsunetaka, H., Hotta, N., Bradak, B., Sakai, Y. (2021): Twenty-five years of geomorphological evolution in the gokurakudani gully (Unzen volcano): Topography, subsurface geophysics and sediment analysis. Geosciences 11(11): 457, https://doi.org/10.3390/geosciences11110457.

Gomez, C. (2013): Tamagawa hanrangen ni okeru tochihifuku no henka to jisin no yure no kankei. Tokyo University CSIS Days 2013, https://doi.org/10.13140/2.1.1181.0880.

Groos, A. R., Bertschinger, T. J., Kummer, C. M., Erlwein, S., Munz, L., Philipp, A. (2019): The potential of low-cost UAVs and open-source photogrammetry software for high-resolution monitoring of Alpine glaciers: a case study from the Kanderfirn (Swiss Alps). Geoscience 9(8): 356, https://doi.org/10.3390/geosciences9080356.

Harpole, J. K., Woods, C. M., Rodebaugh, T. L., Levinson, C. A., Lenze, E. J. (2014): How bandwidth selection algorithms impact exploratory data analysis using kernel density estimation. Psychological Methods 19(3), 428–443, https://doi.org/10.1037/a0036850.

Hartley, R., Zisserman, A. (2004): Multiple view geometry in computer vision. Cambridge University Press, United Kingdom, https://doi.org/10.1017/CBO9780511811685.

Hayakawa, Y. S., Obanawa, H. (2020): Volumetric change detection in bedrock coastal cliffs using terrestrial laser scanning and UAS-based SfM. Sensors 20(12): 3403, https://doi.org/10.3390/s20123403.

Hemmelder, S., Marra, W., Markies, H., De Jong, S. M. (2018): Monitoring river morphology & bank erosion using UAV imagery – A case study of the river Buëch, Hautes-Alpes, France. International Journal of Applied Earth Observation and Geoinformation 73, 428–437, https://doi.org/10.1016/j.jag.2018.07.016.

Hixon, S. W., Lipo, C. P., Hunt, T. L., Lee, C. (2018): Using Structure from Motion Mapping to Record and Analyze Details of the Colossal Hats (Pukao) of Monumental Statues on Rapa Nui (Easter Island). Advances in Archaeological Practice 6(1), 42–57, https://doi.org/10.1017/aap.2017.28.

Iheaturu, C. J., Ayodele, E. G., Okolie, C. J. (2020): An assessment of the accuracy of structure-from-motion (SfM) photogrammetry for 3D terrain mapping. Geomatics, Landmanagement and Landscape 2, 65–82, https://doi.org/10.15576/GLL/2020.2.65.

James, M. R., Robson, S. (2014): Mitigating systematic error in topographic models derived from UAV and ground-based image networks. Earth Surface Processes and Landforms 39(10), 1413–1420, https://doi.org/10.1002/esp.3609.

Javernick, L., Brasington, J., Caruso, B. (2014): Modeling the topography of shallow braided rivers using Structure-from-Motion photogrammetry. Geomorphology 213, 166–182, https://doi.org/10.1016/j.geomorph.2014.01.006.

James, M. R., Robson, S. (2012): Straightforward reconstruction of 3D surfaces and topography with a camera: Accuracy and geoscience application. Journal of Geophysical Research Earth Surface 117(F3), 1–17, https://doi.org/10.1029/2011JF002289.

Kazhdan, M., Hoppe, H. (2013): Screened poisson surface reconstruction. ACM Transactions on Graphics 32(3): 29, https://doi.org/10.1145/2487228.2487237.

King, T. L., Bentley, R. J., Thornton, L. E., Kavanagh, A. M. (2016): Using kernel density estimation to understand the influence of neighbourhood destinations on BMI. BMJ Open 6(2): e008878, https://doi.org/10.1136/bmjopen-2015-008878.

Lague, D., Brodu, N., Leroux, J. (2013): Accurate 3D comparison of complex topography with terrestrial laser scanner: Application to the Rangitikei canyon (NZ). ISPRS Journal of Photogrammetry and Remote Sensing 82, 10–26, https://doi.org/10.1016/j.isprsjprs.2013.04.009.

Liu, X., Lian, X., Yang, W., Wang, F., Han, Y., Zhang, Y. (2022): Accuracy assessment of a UAV direct georeferencing method and impact of the configuration of ground control points. Drones 6(2): 30, https://doi.org/10.3390/drones6020030.

Lochhead, I., Hedley, N. (2022): Evaluating the 3D integrity of underwater structure from motion workflows. Photogrammetric Record 37(177), 35–60, https://doi.org/10.1111/phor.12399.

Long, N., Millescamps, B., Pouget, F., Dumon, A., Lachaussee, N., Bertin, X. (2016): Accuracy assessment of coastal topography derived from UAV images. In Xxiii Isprs Congress, Commission I 41(B1), 1127–134, https://doi.org/10.5194/isprs-archives-XLI-B1-1127-2016.

Lucieer, A., Jong, S. M. D., Turner, D. (2014): Mapping landslide displacements using Structure from Motion (SfM) and image correlation of multi-temporal UAV photography. Progress in Physical Geography: Earth and Environment 38(1), 97–116, https://doi.org/10.1177/0309133313515293.

Matsutani, Y., Tahara, K., Kino, H. (2019): Set-point control of a musculoskeletal system under gravity by a combination of feed-forward and feedback manners considering output limitation of muscular forces. Journal of Robotics and Mechatronics 31(4), 612–620, https://doi.org/10.20965/jrm.2019.p0603.

Mestre-Runge, C., Lorenzo-Lacruz, J., Ortega-Mclear, A., Garcia, C. (2023): An Optimized Workflow for Digital

Surface Model Series Generation Based on Historical Aerial Images: Testing and Quality Assessment in the Beach-Dune System of Sa Ràpita-Es Trenc (Mallorca, Spain). Remote Sensing 15(8): 2044, https://doi.org/10.3390/rs15082044.

Micheletti, N., Chandler, J. H., Lane, S. N. (2015): Investigating the geomorphological potential of freely available and accessible structure-from-motion photogrammetry using a smartphone. Earth Surface Processes and Landforms 40(4), 473–486, https://doi.org/10.1002/esp.3648.

Morgenroth, J., Gomez, C. (2014): Assessment of tree structure using a 3D image analysis technique – A proof of concept. Urban Forestry & Urban Greening 13(1), 198–203, https://doi.org/10.1016/j.ufug.2013.10.005.

Niederheiser, R., Rutzinger, M., Bremer, M., Wichmann, V. (2018): Dense image matching of terrestrial imagery for deriving high-resolution topographic properties of vegetation locations in alpine terrain. International Journal of Applied Earth Observation and Geoinformation 66, 146–158, https://doi.org/10.1016/j.jag.2017.11.011.

Panagiotidis, D., Surový, P., Kuželka, K. (2016): Accuracy of Structure from Motion models in comparison with terrestrial laser scanner for the analysis of DBH and height influence on error behaviour. Journal of Forest Science 62(8), 357–365, https://doi.org/10.17221/92/2015-JFS.

Peppa, M. V., Mills, J. P., Moore, P., Miller, P. E., Chambers, J. E. (2016): Accuracy assessment of a UAV-based landslide monitoring system. ISPRS Archives 41, 895–902, https://doi.org/10.5194/isprs-archives-XLI-B5-895-2016.

Saputra, M. R. U., Markham, A., Trigoni, N. (2018): Visual SLAM and structure from motion in dynamic environments: A survey. ACM Computing Surveys 51(2), 1–36, https://doi.org/10.1145/3177853.

Smith, M. W., Vericat, D. (2015): From experimental plots to experimental landscapes: topography, erosion and deposition in sub-humid badlands from structure-from-motion photogrammetry. Earth Surface Processes and Landforms 40(12), 1656–1671, https://doi.org/10.1002/esp.3747.

Szeliski, R. (2022): Computer vision: algorithms and applications. Springer Nature, Switzerland.

Terefenko, P., Zelaya Wziątek, D., Dalyot, S., Boski, T., Pinheiro Lima-Filho, F. (2018): A high-precision LiDAR-based method for surveying and classifying coastal notches. ISPRS International Journal of Geo-Information 7(8): 295, https://doi.org/10.3390/ijgi7080295.

Tinkham, W. T., Swayze, N. C. (2021): Influence of Agisoft Metashape parameters on UAS structure from motion individual tree detection from canopy height models. Forests 12(2): 250, https://doi.org/10.3390/f12020250.

Tonkin, T. N., Midgley, N. G., Graham, D. J., Labadz, J. C. (2014): The potential of small unmanned aircraft systems and structure-from-motion for topographic surveys: A test of emerging integrated approaches at Cwm Idwal, North Wales. Geomorphology 226, 35–43, https://doi.org/10.1016/j.geomorph.2014.07.021.

Tsunetaka, H., Hotta, N., Hayakawa, Y. S., Imaizumi, F. (2020): Spatial accuracy assessment of unmanned aerial vehicle-based structures from motion multi-view stereo photogrammetry for geomorphic observations in initiation zones of debris flows, Ohya landslide, Japan. Progress in Earth and Planetary Science 7, 1–14, https://doi.org/10.1186/s40645-020-00336-0.

Tsunetaka, H., Shinohara, Y., Hotta, N., Gomez, C., Sakai, Y. (2021): Multi-decadal changes in the relationships between rainfall characteristics and debris-flow occurrences in response to gully evolution after the 1990–1995 Mount Unzen eruptions. Earth Surface Processes and Landforms 46(11), 2141–2162, https://doi.org/10.1002/esp.5148.

Verhoeven, G. (2011): Taking computer vision aloft – archaeological three-dimensional reconstructions from aerial photographs with photoscan. Archaeological Prospection 18(1), 67–73, https://doi.org/10.1002/arp.399.

Vestal, B. E., Carlson, N. E., Ghosh, D. (2021): Filtering spatial point patterns using kernel densities. Spatial Statistics 41: 100487, https://doi.org/10.1016/j.spasta.2020.100487.

Wang, J., Shi, F., Zhang, J., Liu, Y. (2008): A new calibration model of camera lens distortion. Pattern Recognition 41(2), 607–615, https://doi.org/10.1016/j.patcog.2007.06.012.

Wang, L., Liu, G. (2022): Three Camera Lens Distortion Correction Models and Its Application. In 2022 3rd International Conference on Geology, Mapping and Remote Sensing Zhoushan, China, 462–467, https://doi.org/10.1109/ICGMRS55602.2022.9849271.

Wei, Y., Liu, X., Zhao, C., Tomás, R., Jiang, Z. (2021): Observation of surface displacement associated with rapid urbanization and land creation in Lanzhou, Loess Plateau of China with Sentinel-1 SAR Imagery. Remote Sensing 13(17): 3472, https://doi.org/10.3390/rs13173472.

Westoby, M. J., Brasington, J., Glasser, N. F., Hambrey, M. J., Reynolds, J. M. (2012): Structure-from-Motion' photogrammetry: A low-cost, effective tool for geoscience applications. Geomorphology 179, 300–314, https://doi.org/10.1016/j.geomorph.2012.08.021.

Woodget, A. S., Carbonneau, P. E., Visser, F., Maddock, I. P. (2015): Quantifying submerged fluvial topography using hyperspatial resolution UAS imagery and structure from motion photogrammetry. Earth Surface Processes and Landforms 40(1), 47–64, https://doi.org/10.1002/esp.3613.

Zaman, F., Wong, Y. P., Ng, B. Y. (2017): Density-based denoising of point cloud. In 9th International Conference on Robotic, Vision, Signal Processing and Power Applications. Lecture Notes in Electrical Engineering 398, 287–295. Springer Singapore, https://doi.org/10.1007/978-981-10-1721-6_31.

Zambom, A. Z., Dias, R. (2013): A review of kernel density estimation with applications to econometrics. International Economic Review 5(1), 20–42, https://doi.org/10.48550/arXiv.1212.2812.

Zhang, Y., Li, C., Guo, B., Guo, C., Zhang, S. (2021): KDD: A kernel density based descriptor for 3D point clouds. Pattern Recognition 111: 107691, https://doi.org/10.1016/j.patcog.2020.107691.

Zhao, Q., Gao, X., Li, J., Luo, L. (2021): Optimization algorithm for point cloud quality enhancement based on statistical filtering. Journal of Sensors 2021(1): 7325600, https://doi.org/10.1155/2021/7325600.